A High-Sensitivity Magnetic Tactile Sensor With a Structure-Optimized Hall Sensor and a Flexible Magnetic Film

Xuejiao Li, Runyi Deng, Wenlong Jiao, Shizhen Xu, Huikai Xie, *Fellow, IEEE*, Dong Han, and Xiaoyi Wang, *Member, IEEE*

***Abstract*—This article presents a high-sensitivity magnetic tactile sensor comprising a dipole magnetic film and a *z*-axis Hall sensor. The tactile sensor primarily focuses on pressure response along the *z*-axis, minimizing interference from magnetic fields in other axes and thereby simplifying signal processing complexity. To enhance the overall performance of the tactile sensor, a qualitative analysis and structural optimization are conducted on both the magnetic film and the Hall sensor. The magnetic film is optimized by comparing different thicknesses and magnetic powder mass fractions, and the Hall sensor undergoes structural optimization through a comparative analysis of different length-to-width (*L*/*W*) ratios. By embedding the Hall sensor into the printed circuit board (PCB), we can ensure a snug fit with the ultrathin flat magnetic film, resulting in an advantageous packaging effect. Employing these approaches, we substantially improve sensitivity, measuring at 5.92 Gs/N, surpassing the sensitivity level (about 0.17 Gs/N) reported in previous works by one order of magnitude. Finally, the device performs comprehensive characterizations, revealing excellent properties, including low hysteresis (6.82%), the rapid response time (<2 ms), remarkable stability (0.09%), and high repeatability (0.48%). This research will actively promote the development of tactile sensors, which offer substantial applications in robotics, health monitoring, and electronic skin devices.**

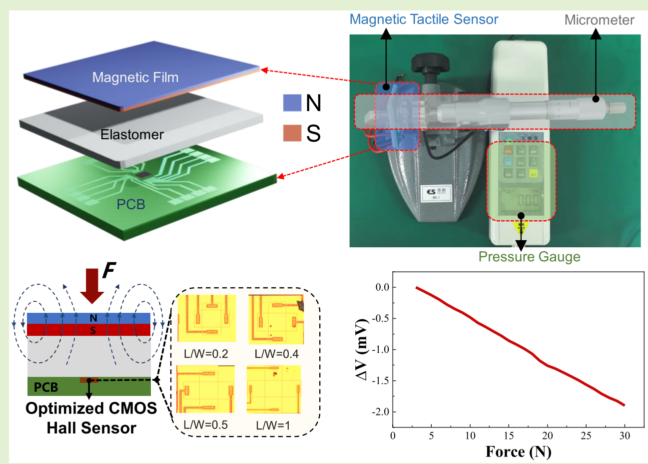

***Index Terms*—CMOS Hall sensor, dipole magnetic film, high sensitivity, magnetic tactile sensor, structural optimization.**

Manuscript received 14 March 2024; accepted 27 March 2024. Date of publication 16 April 2024; date of current version 15 May 2024. This work was supported in part by the National Natural Science Foundation of China under Grant 62304023 and Grant 52105072, in part by the Natural Science Foundation of Chongqing under Grant 2022NSCQ-MSX5423, and in part by Beijing Institute of Technology Research Fund Program for Young Scholars under Grant XSQD-202206004. The associate editor coordinating the review of this article and approving it for publication was Prof. Guiyun Tian. *(Xuejiao Li and Runyi Deng contributed equally to this work.) (Corresponding authors: Dong Han; Xiaoyi Wang.)*

Xuejiao Li, Shizhen Xu, and Xiaoyi Wang are with the School of Integrated Circuits and Electronics, Beijing Institute of Technology, Beijing 100081, China (e-mail: xiaoyiwang@bit.edu.cn).

Runyi Deng and Dong Han are with the School of Mechanical Engineering, Zhejiang University, Hangzhou, Zhejiang 310027, China (e-mail: dong_han@zju.edu.cn).

Wenlong Jiao is with the BIT Chongqing Institute of Microelectronics and Microsystems, Chongqing 400030, China (e-mail: jiaowl@cimems.com).

Huikai Xie is with the School of Integrated Circuits and Electronics, Beijing Institute of Technology, Beijing 100081, China, and also with the BIT Chongqing Institute of Microelectronics and Microsystems, Chongqing 400030, China.

Digital Object Identifier 10.1109/JSEN.2024.3385299

I. Introduction

TACTILE sensors play a vital role in human tactile perception and have numerous applications in human life. For instance, tactile sensors have been gradually applied to robotic systems for environmental perception and dexterous operation. By possessing the capability, robots acquire a sense of touch, facilitating adaptive grasping and enhancing human–robot interaction [1], [2]. In addition, tactile sensors have been utilized to implement electronic skin, which can mimic tactile sensations [3], [4] and monitor physical conditions to facilitate health detection [5], [6]. They measure and quantify the electrical signals generated by human activities, enabling the monitoring of various indicators of human health [7], [8], [9], [10]. To date, different sensing types of tactile sensors, including magnetic [11], [12], [13], [14], [15], [16], [17], [18], [19], piezoresistive [20], [21], [22], and capacitive [23], [24], [25] sensors, have been developed. Magnetic tactile sensors can provide rich information dimensions, extracting

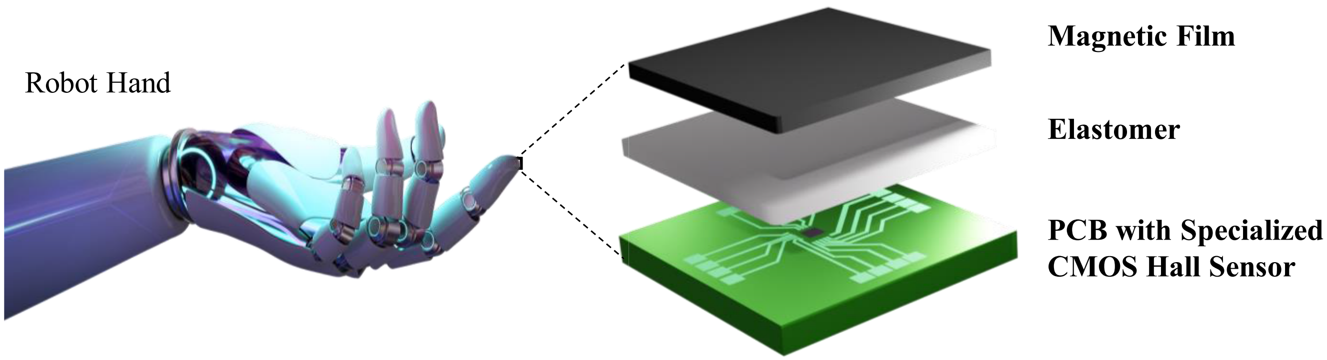

Fig. 1. Illustration of the magnetic tactile sensor. Robot hand image source: pixabay.com.

force information including magnitude, direction, and position through magnetic field information in three directions. Moreover, magnetic tactile sensors have higher stability and lower hysteresis than resistive types, better linearity than capacitive types, and a wider range of force types than piezoelectric types and are less susceptible to external environmental influences than optical types. Finally, magnetic tactile sensors have the advantages of a simple structure and are easy to use.

Currently, many researchers have carried out extensive studies to improve the performance of magnetic tactile sensors. For example, Yan et al. [26] reported a work using a proper design of the magnetization direction in the flexible magnetic film and variable transformation by theoretical calculations to solve the coupling problem between normal force and shear force. Yan et al. [26] and Hu et al. [27] proposed a method utilizing sensor arrays and algorithms to enhance the spatial resolution of tactile sensors. The unambiguous discrimination between tactile and touchless interactions has also been successfully achieved through the rational design of the structure, such as air gaps and pyramid-shaped extrusions [13].

To improve the pressure/force perception performance, sensitivity was also focused on by some reported works. The most common approach to enhancing sensitivity is by modifying the magnetization method and the structure of magnetic films, thereby increasing the surface magnetic field strength. Methods to improve the performance of flexible magnetic films include origami [28], [29], folding [30], [31], microstructure [32], [33], [34], and Halbach magnetization [26], [35]. These methods significantly increase the surface magnetic field strength.

However, methods to enhance the surface magnetic field strength of the magnetic film invariably complicate the surface magnetic field strength distributions, which cause magnetic field component signals in the three directions of x, y, and z and increase signal processing difficulty. In addition, recent research relies more on experiments to determine the dimensional parameters of magnetic films, but there is a lack of theoretical or numerical optimization. Another key element of the magnetic tactile sensor is the Hall sensor. Currently, commercially available Hall sensors are widely utilized, but a mismatch occurs due to the fixed size and packaging of Hall sensors [27], reducing sensitivity and limiting their effectiveness in industrial applications. There is an urgent need to qualitatively analyze the most basic combination of a magnetic film and a Hall sensor and conduct structural optimization analysis to promote follow-up research.

This article introduces a tactile sensor enhancing performance through optimized design and packaging. Composed of a dipole magnetic film and a z-axis Hall sensor, the tactile sensor mainly focuses on pressure response along the z-direction, minimizing interference from magnetic fields in other axes and, thereby, simplifying signal processing complexity. To enhance the overall performance of the tactile sensor, the magnetic film and Hall sensor are optimized, respectively. The magnetic film was optimized by comparing the thicknesses and the mass fractions. By manufacturing Hall sensors in different sizes, the optimal performance is achieved by selecting the sensor size that demonstrates the best performance for tactile sensor applications. Simultaneously, the Hall sensors are embedded in the printed circuit board (PCB) during packaging to ensure a precise fit and optimal integration. In summary, these methods can enhance the sensitivity of tactile sensors without complicating the magnetic field. Furthermore, we have filled a gap in structural parameters and performance optimization of dipole magnetic film and z-axis sensor cooperation. The qualitative analysis and performance optimization of this most basic type of magnetic tactile sensor will benefit subsequent research of complex structure magnetic film and multiple-axis Hall sensors.

II. Design and Fabrication

As illustrated in Fig. 1, the tactile sensor consists of three parts: the top layer is a flexible magnetic film, which generates a magnetic field in a specific direction, and the distribution of the magnetic field changes when an external force is applied. The middle layer is an elastomer of Ecoflex 00-30 (1 mm thickness), which is utilized to increase a certain degree of deformation so that the magnetic field change increases. The bottom layer is a PCB with a Hall sensor mounted, which senses the change in the magnetic field and, thus, outputs corresponding electrical values.

When an external force F is applied to the flexible magnetic film, the magnetic film produces deformation, which will result in the displacement of permanent magnetic particles, and the magnetic flux under the magnetic film changes. The Hall sensor senses changes in the magnetic field due to the Hall effect and outputs a corresponding Hall voltage.

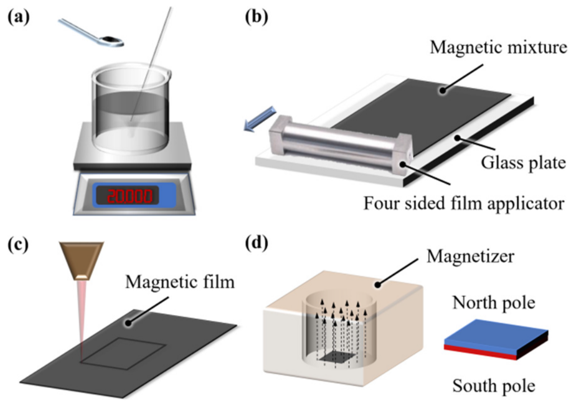

Fig. 2. Fabrication of dipole magnetic film. (a) Mix NdFeB powder and Dragon Skin 10 NV. (b) Coating film. (c) Laser cutting. (d) Magnetization.

Fig. 2 shows the fabrication of the dipole magnetic films. The magnetic films comprise magnetic powder NdFeB and Dragon skin 10 NV (Smooth-On, Macungie, PA). First, we mixed Part A and Part B of Dragon skin 10 NV in the 1:1 mass ratio and then added NdFeB with an average size of 38 μm (LW-N 12-9, Guangzhou Xinnuode Transmission Parts Company Ltd., China) with different mass fractions (40, 50, and 60 wt.%).

The mixture was stirred evenly and poured onto a glass plate, and then a film applicator made it into a film. After curing, the laser cutting machine cut the film into 2 $\times$ 2 cm. Finally, the magnetizer magnetized the magnetic film at 3 T in the direction of thickness.

Fabricated using a standard 0.18-μm CMOS technology, Hall sensors are made in a cross-shape for the best performance. Fig. 3(a) exhibits a cross-shaped Hall plate's typical plan and side sectional views. First, an N-well layer with a cross-like shape was implemented on a p-type substrate to form the device's active region. Moreover, four same contact regions with a highly doped N+ implantation layer were formed to reduce contact resistance. Finally, to decrease the flicker noise induced by carrier surface recombination, a heavily doped P+ implanting layer covered the surface of the device. To enhance the performance, the Hall sensor is structurally optimized through a comparative analysis of different length-to-width (L/W) ratios. To ensure the structure is practical, Hall sensors with different L/W ratios are simulated by COMSOL Multiphysics, as shown in Fig. 3(b). Here, N-type silicon was chosen as the material, whose conductivity was set to 100 S/m. The physical field was selected as "current," whose conduction model was chosen as "Hall effect" and the Hall coefficient was set to about $(-16.425 \times 10^3)\mathrm{m}^3/(\mathrm{s}\cdot\mathrm{A})$. Then, L/W is scanned parametrically from 0.1 to 1.2 in steps of 0.05, and the trend of Hall voltage with L/W is counted. It reveals that the simulated sensitivity goes up rapidly with the increase in L/W and a maximum value is achieved at $L/W \approx 0.4$. Subsequently, it decreases slowly with L/W increasing. The trend can be explained by the theoretical formula [36]

$$S_H \approx \frac{G}{2\frac{L}{W}+\frac{2}{3}}\mu_H \tag{1}$$

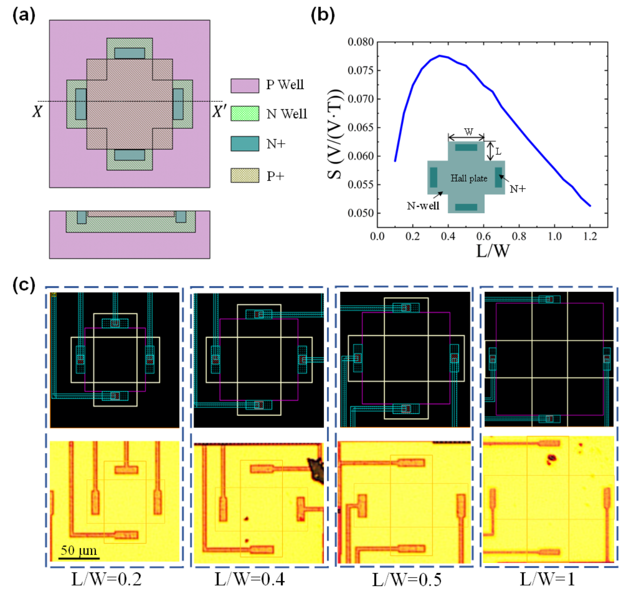

Fig. 3. (a) Top and side views of the Hall sensor structure. (b) Simulation results of Hall sensor sensitivity concerning L/W. (c) Four different sizes of Hall sensors. The top row is the layout drawn by cadence software, and the bottom row is the physical drawing obtained by metallurgical microscopy.

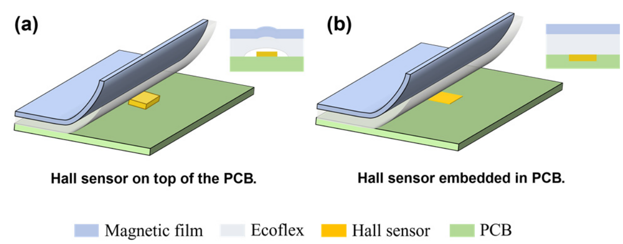

Fig. 4. Position of the Hall sensor relative to the PCB. (a) Hall sensor on top of the PCB. (b) Hall sensor embedded in PCB.

where G and μ_H denote the geometric factor of the Hall device and Hall mobility, respectively. An analytical expression of G for a cross-like Hall plate operating is derived by

$$G = 1 - 1.044\exp\left(-3.142\frac{L}{W}\right). \tag{2}$$

Based on the results, four specific sizes of Hall sensors are chosen for the fabrication process. Fig. 3(c) displays the four cross-like Hall plates with L/W ratios of 0.2, 0.4, 0.5, and 1, respectively. The cross width (W) of all the Hall plates is designed to be 50 μm.

To ensure a flat fit between the PCB and the magnetic film, the Hall sensor was embedded within the PCB during the packaging process instead of simply glued on top of the PCB. This embedded approach allows for a more precise and seamless integration between the PCB and the magnetic film, enhancing the overall performance and reliability of the sensor. Fig. 4 illustrates the comparison of the packaging methodology employed in this article with other studies that utilize commercial Hall sensors. It highlights the distinctive packaging approach adopted in this research, showcasing its advantages and distinguishing features compared to previous works.

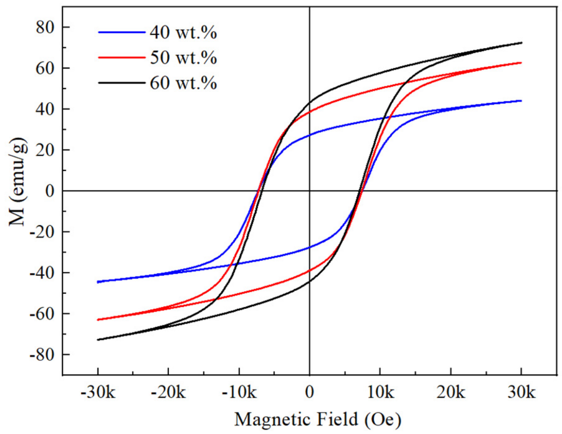

Fig. 5. M-H curves of NdFeB with different mass fractions.

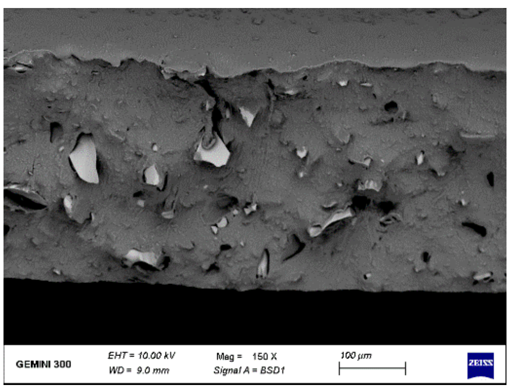

Fig. 6. SEM image of the magnetic material.

III. Results and Discussion

A. Magnetic Film

1) Magnetic Properties: The performance characterization of flexible materials is extremely important [37]. The magnetic properties of the materials were characterized by a physical property measurement system (PPMS-9T, Quantum Design). Magnetization versus magnetic field (M-H) curves of NdFeB with different mass fractions are shown in Fig. 5. It shows that M_r increases with the increasing of mass fraction, which is up to the maximum when the content of NdFeB is 60 wt.%: $M_r = 43.4$ emu/g.

Fig. 6 shows the distribution of 60 wt.% NdFeB particles in Dragon Skin 10 NV, using a scanning electron microscopy (SEM, ZEISS G300, Zeiss, Germany).

2) Simulation Optimization: The magnetic field distribution of the magnetic film mainly depends on the magnetic properties and the shape. For the block shape of magnetic film, the magnetic field above the surface B_h is calculated as this equation [38]

$$B_h = \frac{B_r}{\pi}\left[\arctan\frac{lw}{2h\sqrt{4h^2+l^2+w^2}} - \arctan\frac{lw}{2(t+h)\sqrt{4(t+h)^2+l^2+w^2}}\right] \quad (3)$$

where l is the film's length, w is the width, t is the thickness of the magnet, and h is the height above the magnet's surface. These parameters are related to geometry. This article sets l and w to constant (2 cm), mainly studying the influence of t and h.

The magnetic remanence B_r is the magnetic induction or magnetic flux density remaining in zero field ($H = 0$) after an external magnetic field is applied, which is enough to achieve saturation. It is relevant to the performance of the material itself and is defined as

$$B = \mu_0 (H + M) \quad (4)$$

$$B_r = \mu_0 M_r \quad (5)$$

where the constant $\mu_0 (4\pi \times 10^{-7} \mathrm{N \cdot A^{-2}})$ is the vacuum magnetic permeability, B represents the density of magnetic flux, H is magnetic field intensity, and M is the magnetization. The remnant magnetization M_r is measured by an instrument such as a physical property measurement system.

In the simulation conducted using COMSOL Multiphysics, magnetic field components in the x-, y-, and z-axes (B_x, B_y, B_z) are obtained and visualized in Fig. 7(a)–(c). The magnetization is oriented along the thickness direction in this study. The analysis reveals that B_x and B_y are prominently concentrated at the edges of the magnetic film. In contrast, B_z is more uniformly distributed across the surface. Given this distribution, the study selects a z-axis Hall sensor to capture the characteristics of the magnetic field.

According to the calculation formula, we set the thickness of the magnetic film t and the height from the surface of the magnetic film h as variables for parameter optimization, and the mass fraction of NdFeB is 60 wt.%. $t_1 = 0.1$ mm, $t_2 = 0.2$ mm, $t_3 = 0.3$ mm, $t_4 = 0.4$ mm, and $t_5 = 0.5$ mm; $h_1 = 0.1$ mm, $h_2 = 1$ mm, and $h_3 = 10$ mm. Parameter simulation results are shown in Fig. 7(d)–(f). To control the thickness of the magnetic film in the submillimeter range and ensure sufficient sensitivity, 0.5 mm is chosen as the upper limit for the simulation. As the value of t increases, the magnetic field intensity increases; as the value of h increases, the magnetic field intensity decreases. The mean value of B_z is 2.3 mT (t_5, h_1).

3) Experimental Results: The surface magnetic field automatic testing system (TY2100, TUNKIA, China) tests the magnetic films with different mass fractions and thicknesses. Fig. 8 illustrates that increasing the magnetic field strength is considered from two aspects: increasing the thickness and the mass fraction of magnetic powder. When the mass fraction of magnetic powder is 60 wt.% and the thickness of the magnetic film is 500 μm, the maximum average magnetic field value at the center is 2.59 mT.

Tensile Young's modulus of different mass fractions is shown in Fig. 9, which was tested by a universal testing machine (Z020, ZwickRoell, Germany). As the mass fraction increases, Young's modulus increases. The tensile Young's modulus of 40 wt.% NdFeB (thickness of 300 μm) is 0.71 MPa, and the 60 wt.% NdFeB is 1.14 MPa. As depicted in Fig. 9, both linearity and strain range decrease as the mass fraction of magnetic powder in the silicone elastomer composite increases. One of the factors is the effect of particle agglomeration. As the mass fraction of magnetic powder increases, there is a higher likelihood of particle agglomeration

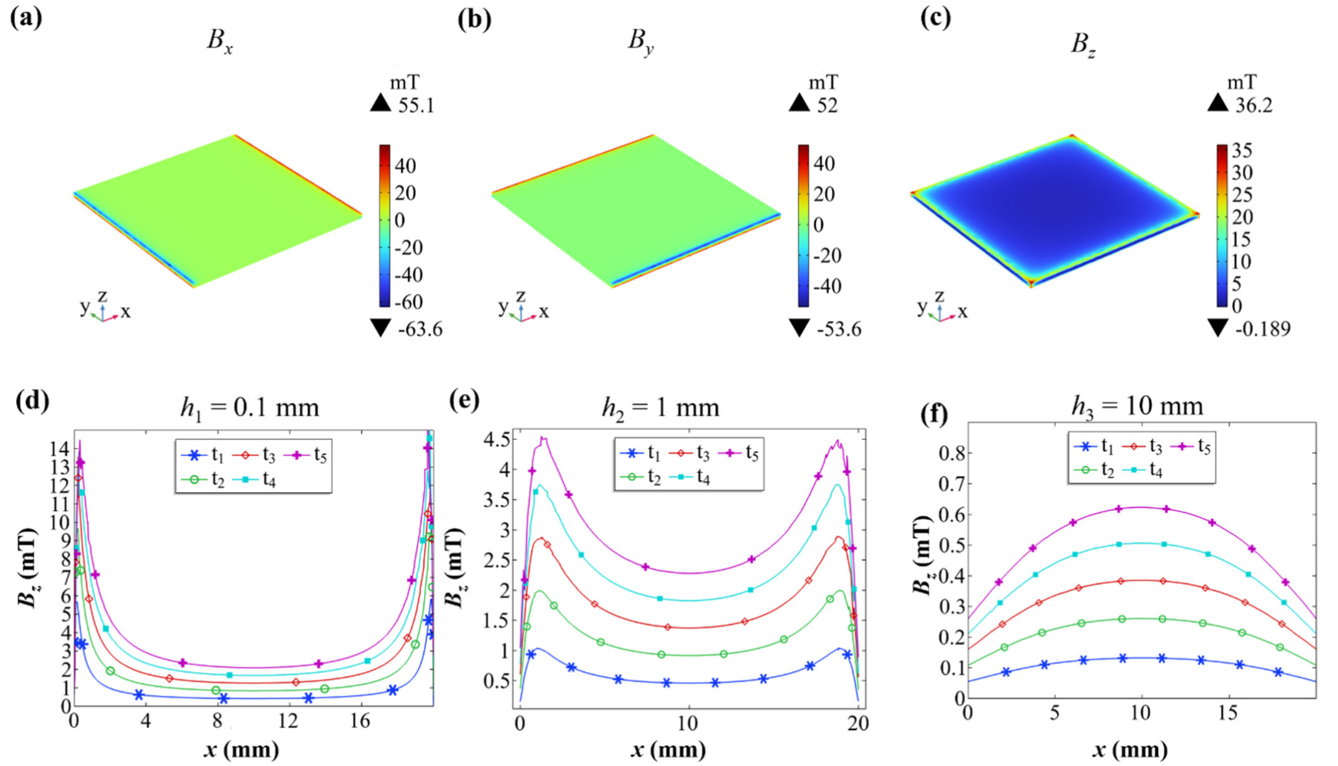

Fig. 7. Magnetic film simulation and parameter optimization. (a) Distribution of B_x. (b) Distribution of B_y. (c) Distribution of B_z. (d) Curves of B_z at h_1. (e) Curves of B_z at h_2. (f) Curves of B_z at h_3.

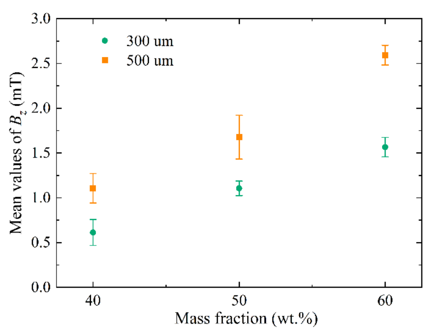

Fig. 8. Test of the surface magnetic field.

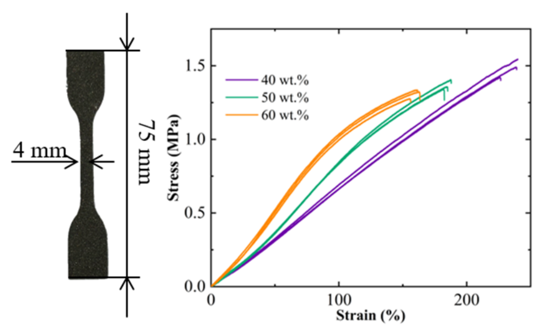

Fig. 9. Test of tensile Young's modulus.

within the elastomer matrix. This agglomeration leads to a nonuniform distribution of particles, resulting in localized areas of higher stiffness and reduced elasticity. Consequently, the material exhibits less linear behavior as the strain increases. Besides, we also need to consider the effect of the reduction of the polymer network connectivity. With higher mass fractions of magnetic powder, the polymer network within the elastomer matrix may become disrupted. This disruption weakens the connectivity between polymer chains, leading to reduced elasticity and increased susceptibility to deformation at higher strains. As a result, the material's ability to maintain linearity in stress–strain behavior diminishes.

B. Hall Sensor

1) Geometry Optimization for Maximum Sensitivity: The sensitivity of a Hall sensor refers to the degree of change in the output voltage in response to variations in the magnetic field. For sensitivity property characterization, the relative magnetic field density was tuned from 0 to 60 mT, which is enough to measure the magnetic field generated by the magnetic film. The output voltage of the hall sensor at the relative magnetic field density of 0 T was set as the base value, and the output voltage change is plotted in Fig. 10(a). The following equation calculates the sensitivity value:

$$S_H = \frac{V_H}{B_z \cdot V_{\mathrm{BIAS}}} \, (\%/\mathrm{T}) \tag{6}$$

where S_H is the sensitivity of the Hall sensor, B_z is the magnetic field applied to the Hall sensor, and V_H and V_{BIAS} represent the output voltage and bias voltage, respectively.

The Hall sensors of four different L/W ratios are compared in Fig. 10(a), and it is experimentally demonstrated a

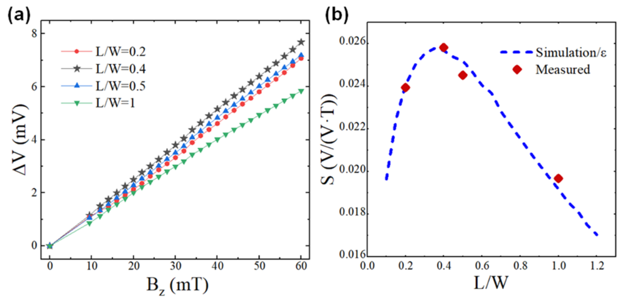

Fig. 10. (a) Output comparison of different L/W Hall sensors under different magnetic fields. (b) Comparison of Hall sensor sensitivity obtained from simulation and experiment, respectively.

maximum sensitivity of 2.5 %/T when the cross L/W ratio of the Hall plate is about 0.4.

As illustrated in Fig. 10(b), the simulation results are consistent with the changing trend of the experimental results.

2) Offset Cancellation: Hall misalignment is a condition in which a Hall device has an electrical potential difference across the sensing electrodes of the device even when no magnetic field is applied. Misalignment is mainly caused by defects in the device fabrication process, such as geometrical errors in the device structure, uneven doping concentration, uneven thickness, and asymmetry of the contact electrodes. In addition, Hall devices are subjected to mechanical stress, piezoresistive effects, thermal expansion and contraction during packaging, and other external factors can also cause misalignment.

The rotating current technique can remove the bias voltage. Fig. 11(a) and (b) illustrates the two-phase rotating current technique, and ΔR characterizes the offset. The offset voltage can be effectively eliminated by rotating the input and output states of the four ports and then summing or subtracting the outputs. When the Hall device is operating, as shown in Fig. 11(a), the bias current flows into the Hall device from the top to the bottom, and the following equation calculates the potential difference between the left and right ports:

$$V_{O1} = V_{H1+} - V_{H1-} = V_{\mathrm{Hall}} + \left(\frac{1}{2} - \frac{R}{2R+\Delta R}\right) V_{\mathrm{BIAS}} \quad (7)$$

when the Hall device is operating, as shown in Fig. 11(b), the bias current flows into the Hall device from the left to the right, and the potential difference between the top and bottom ports is calculated by the following equation:

$$V_{O2} = V_{H2-} - V_{H2+} = -V_{\mathrm{Hall}} + \left(\frac{1}{2} - \frac{R}{2R+\Delta R}\right) V_{\mathrm{BIAS}}. \quad (8)$$

The absolute values of the Hall voltage and the out-of-phase voltage produced by the same Hall device in different phases should be the same, so subtracting the output voltages of the two cases before and after can eliminate the out-of-phase voltage

$$V_O = V_{O1} - V_{O2} = 2V_{\mathrm{Hall}}. \quad (9)$$

The four-phase rotating current technique was applied to reduce the offset voltage. As illustrated in Fig. 11(c), the offset voltage is reduced by 94.75% compared to the original result after the rotating current technique.

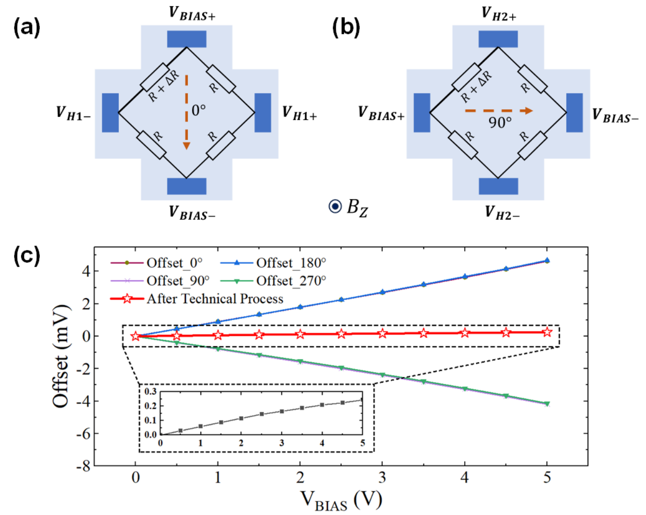

Fig. 11. Characterization of rotating current technique. (a) State of the Hall sensor at 0°. (b) State of the Hall sensor at 90°. (c) Comparison of offset voltage before and after treatment.

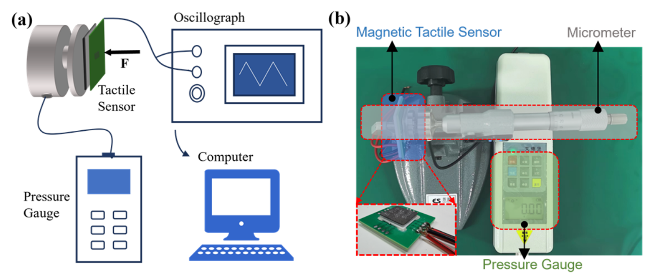

Fig. 12. (a) Schematic of the test setup for the tactile sensor. (b) Picture of the test setup for the tactile sensor. The tactile sensor is shown in the lower left corner.

C. Magnetic Tactile Sensor

In this article, the performance of the tactile sensor is evaluated through sensitivity, hysteresis, response time, and so on. During response time, step signal output, repeatability, and stability testing, the Hall output voltage was amplified approximately 100 times by an instrumentation amplifier to avoid the oscilloscope bottom noise masking small signals. When it comes to the test setup, by applying force to each other with a tactile sensor and a pressure gauge, the pressure gauge detects the amount of force, and the tactile sensor outputs the voltage, which is captured by a multimeter and an oscilloscope, as illustrated in Fig. 12.

1) Sensitivity Test: Sensitivity is an important property of a tactile sensor. Higher sensitivity indicates better sensor performance. The corresponding output voltage was tested from 3 to 30 N during the sensitivity test, as shown in Fig. 13(a) and (b). The following equation calculates the sensitivity value:

$$S = \frac{|V_{F_2} - V_{F_1}|}{F_2 - F_1}\,(V/N) \quad (10)$$

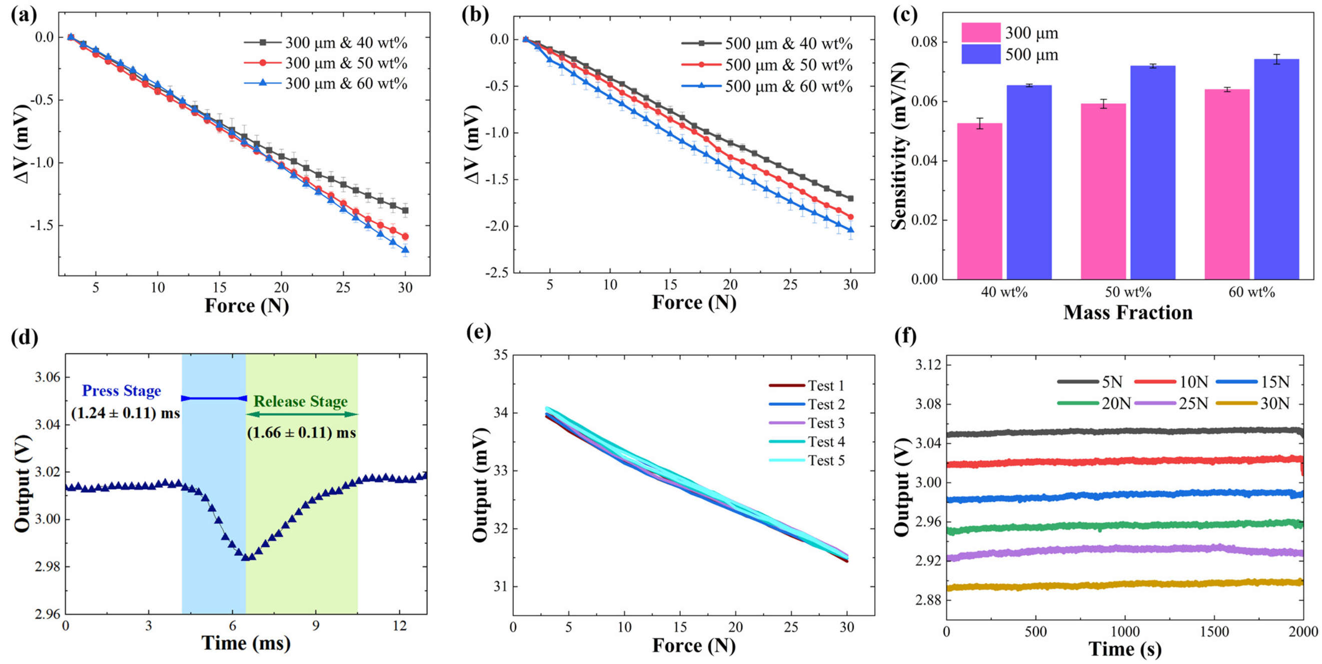

Fig. 13. Characterization of tactile sensor performance. Output Comparison of tactile sensors composed of different mass fractions with (a) 300 μm thickness and (b) 500 μm thickness, respectively. (c) Sensitivity comparison of tactile sensors corresponding to different types of magnetic films. (d) Response time characterization. (e) Hysteresis characterization. (f) Stability characterization.

Different tactile sensors corresponding to different magnetic films were measured. Fig. 13(a) and (b) illustrates a comparison of the outputs of tactile sensors consisting of magnetic films with different thicknesses and mass fractions. As shown in Fig. 13(c), the higher the mass fraction of the magnetic powder or the thicker the magnetic film, the stronger the magnetic field on the surface of the magnetic film, and the greater the change in the magnetic field when subjected to pressure, which ultimately results in a higher sensitivity of the tactile sensor, consistent with Fig. 8. Each set of experiments was repeated three times, and the error bars in Fig. 13(a) and (b) represent the data fluctuations in the three tests. The errors can be attributed to factors such as uneven magnetic film powders, mechanical noise, and human testing errors. The results indicate that the tactile sensor achieves its highest sensitivity when the magnetic film has a thickness of 500 μm and a mass fraction of 60 wt.%. In this configuration, the sensitivity value reaches its maximum value of 0.074 mV/N (5.92), which is one order of magnitude higher than previous papers, and the measurement range is larger [27].

2) Transient Test: The response behavior of the tactile sensor was characterized by conducting a test where a 15-mm-diameter ball weighing 14 g was dropped five times onto the sensor at a distance of 3 cm. As illustrated in Fig. 13(d), the response time of the applying and releasing force process is (1.24 $\pm$ 0.11) and (1.66 $\pm$ 0.11) ms, respectively.

3) Hysteresis Test: During the application of force, the result is a certain hysteresis due to the elastic recovery properties of the elastomer and the magnetic film. For hysteresis property characterization, the relative force was tuned from 3 to 30 N and then returned to 3 N for five tests, as illustrated in Fig. 13(e). The following equation can calculate the hysteresis value:

$$H = \frac{V_{A\_F} - V_{R\_F}}{V_{F=3N} - V_{F=30N}}\% \tag{11}$$

where V_{A_F} and V_{R_F} are the voltage values tested at a certain F value in the applying and releasing force processes, respectively. The maximum hysteresis value of the tactile sensor is 6.82%.

4) Stability Test: The stability of the tactile sensor was characterized by different constant force values ranging from 5 to 30 N, as shown in Fig. 13(f). The stability index coefficient of variation (C_v) of the voltage change is characterized via the following equation:

$$C_v = \frac{\sigma}{\mu} \tag{12}$$

where σ is the standard deviation of a set of voltage values and μ is their mean. The C_v values at the relative force of 5, 10, 15, 20, 25, and 30 N are 0.04%, 0.06%, 0.09%, 0.07%, 0.09%, and 0.07%, respectively. The results show long-term stability.

5) Step Signal Output: Fig. 14(a) exhibits a step signal under different relative force values in applying force from 5 to 17 N and releasing force from 17 to 5 N.

6) Repeatability Test: To characterize the repeatability of the device, the dynamic response was conducted with force ramp-up and ramp-down circles, as shown in Fig. 14(b). A range of force increases (from 5 to 20 N) and force decreases (from 20 to 5 N) was monitored over 200 cycles. The variation of the repeatability (V_r) is calculated to describe the repeatability of the sensor via the following equation:

$$V_r = \frac{\left|V_{\text{peak}} - V_{\text{peak\_average}}\right|}{V_{\text{range}}}\% \tag{13}$$

TABLE I
PERFORMANCE COMPARISON OF SENSORS WITH SIMILAR FUNCTIONS

	Fabrication Process	Sensitivity*	Hysteresis*	Repeatability	Range	Response
Yan [26]	MLX90393(Melexis)	0.01 kPa^{-1}	2.19%	Over 3000 cycles@ 110 kPa	120kPa	15ms
Hu [27]	Wit, RM3100	0.17 Gs/N	N/A	Over5200 cycles@1.0N	N/A	15ms-35ms
Hellebrekers [12]	MLX90393(Sparkfun)	N/A	N/A	N/A	2.5N	N/A
Our work	standard 0.18-μm CMOS technology	5.92 Gs/N (0.08 kPa^{-1})	6.82%	0ver 200 cycles@15N	30N(75 kPa)	$<$2ms

*Sensitivity and hysteresis were calculated from the data in the reference papers.

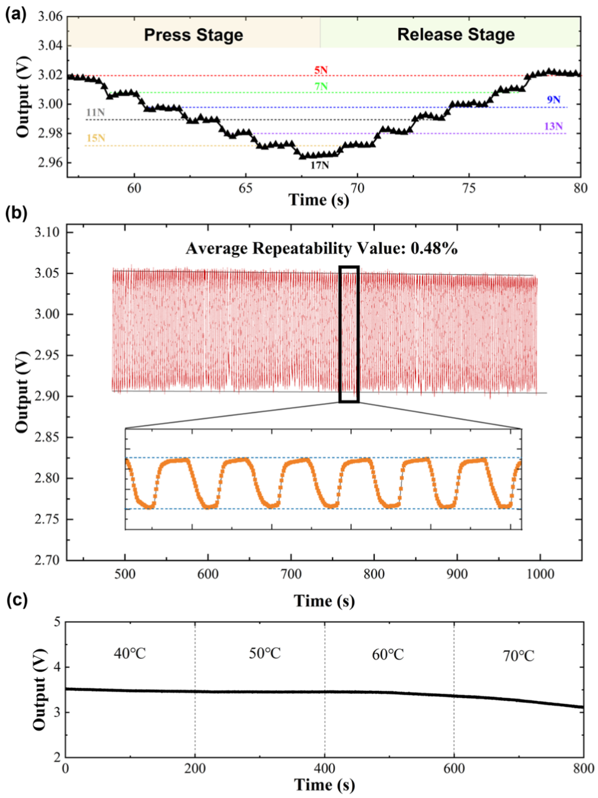

Fig. 14. (a) Step output characterization of the tactile sensor. (b) Repeatability of the tactile sensor with the periodical force change from 5 to 20 N. (c) Temperature effects on tactile sensors.

where V_{peak} is the peak voltage change of each cycle and V_{range} is the peak difference of each voltage change period. Based on this definition, the variation of the repeatability of the device is calculated with the average value V_{r_ave} of 0.48%.

7) Thermal Effect Test: To characterize the response to temperature, the output at different temperatures was tested. As shown in Fig. 14(c), the output was tested at four temperatures (40 °C, 50 °C, 60 °C, and 70 °C), each lasting for 200 s. During 40 °C–60 °C, it is relatively stable, and when the temperature rises to 70 °C, the output drops slightly as the alignment of the magnetic domains is affected, and the magnetic properties are weakened.

IV. CONCLUSION

This article introduces a high-sensitivity magnetic tactile sensor that consists of a dipole magnetic film and a z-axis Hall sensor. The tactile sensor's optimal performance is achieved through qualitative analysis and structural optimization of the magnetic film and Hall sensor. By manipulating the magnetic film's thickness and mass fraction, the tactile sensors' performance is systematically analyzed, revealing that increasing the thickness and mass fraction leads to higher sensitivity of the tactile sensor. To improve the performance of the Hall sensor, a structural optimization process is conducted by comparing different L/W ratios. This comparative analysis determines the optimal L/W ratio, resulting in enhanced performance of the Hall sensor. The structural optimization allows for improved sensitivity and overall effectiveness of the sensor in its intended application. Moreover, the Hall sensor was embedded within the PCB to achieve a precise and secure integration, ensuring a snug fit with the ultrathin flat magnetic film. Employing these approaches, we substantially improve sensitivity, measuring at 5.92 Gs/N, surpassing the sensitivity level (about 0.17 Gs/N) reported in previous works by one order of magnitude. The performance of the sensor compared to other sensors with the same function is summarized in Table I. It is worth mentioning that the devices are outstanding in terms of sensitivity and response. In conclusion, the approach can effectively avoid increasing the complexity of the magnetic field and reduce the difficulty of processing the signal. In addition, it can fill the gap in analyzing the effect of size on device performance through quantitative analysis. However, this method only stays at the enhancement of sensitivity with less information dimension. In terms of future improvements, it is intended to incorporate aspects such as three-axis force decoupling and position sensing to make the tactile sensor with more comprehensive performance.

REFERENCES

[1] Y. Guo, Z. Guo, M. Zhong, P. Wan, W. Zhang, and L. Zhang, "A flexible wearable pressure sensor with bioinspired microcrack and interlocking for full-range human–machine interfacing," *Small*, vol. 14, no. 44, Nov. 2018, Art. no. 1803018, doi: 10.1002/smll.201803018.

[2] T.-H. Chang et al., "Stretchable graphene pressure sensors with Shar-Pei-like hierarchical wrinkles for collision-aware surgical robotics," *ACS Appl. Mater. Interface*, vol. 11, no. 10, pp. 10226–10236, Mar. 2019, doi: 10.1021/acsami.9b00166.

[3] D. J. Lipomi et al., "Skin-like pressure and strain sensors based on transparent elastic films of carbon nanotubes," *Nature Nanotechnol.*, vol. 6, no. 12, pp. 788–792, Dec. 2011, doi: 10.1038/nnano.2011.184.

[4] S. Gong et al., "A wearable and highly sensitive pressure sensor with ultrathin gold nanowires," *Nature Commun.*, vol. 5, no. 1, p. 3132, Feb. 2014, doi: 10.1038/ncomms4132.

[5] R. Mao et al., “3-D graphene aerogel sphere-based flexible sensors for healthcare applications,” *Sens. Actuators A, Phys.*, vol. 312, Sep. 2020, Art. no. 112144, doi: 10.1016/j.sna.2020.112144.

[6] Y. Wang, M. Chao, P. Wan, and L. Zhang, “A wearable breathable pressure sensor from metal-organic framework derived nanocomposites for highly sensitive broad-range healthcare monitoring,” *Nano Energy*, vol. 70, Apr. 2020, Art. no. 104560, doi: 10.1016/j.nanoen.2020.104560.

[7] X. Li et al., “Ultracomfortable hierarchical nanonetwork for highly sensitive pressure sensor,” *ACS Nano*, vol. 14, no. 8, pp. 9605–9612, Aug. 2020, doi: 10.1021/acsnano.9b10230.

[8] X. Lin, S. Gao, T. Fei, S. Liu, H. Zhao, and T. Zhang, “Study on a paper-based piezoresistive sensor applied to monitoring human physiological signals,” *Sens. Actuators A, Phys.*, vol. 292, pp. 66–70, Jun. 2019, doi: 10.1016/j.sna.2019.04.009.

[9] S. Chen et al., “Hierarchical elastomer tuned self-powered pressure sensor for wearable multifunctional cardiovascular electronics,” *Nano Energy*, vol. 70, Apr. 2020, Art. no. 104460, doi: 10.1016/j.nanoen.2020.104460.

[10] X. Lin et al., “Flexible piezoresistive sensors based on conducting polymer-coated fabric applied to human physiological signals monitoring,” *J. Bionic Eng.*, vol. 17, no. 1, pp. 55–63, Jan. 2020, doi: 10.1007/s42235-020-0004-9.

[11] Y. Jiang et al., “A flexible and ultra-highly sensitive tactile sensor through a parallel circuit by a magnetic aligned conductive composite,” *ACS Nano*, vol. 16, no. 1, pp. 746–754, Jan. 2022, doi: 10.1021/acsnano.1c08273.

[12] T. Hellebrekers, O. Kroemer, and C. Majidi, “Soft magnetic skin for continuous deformation sensing,” *Adv. Intell. Syst.*, vol. 1, no. 4, Aug. 2019, Art. no. 1900025, doi: 10.1002/aisy.201900025.

[13] J. Ge et al., “A bimodal soft electronic skin for tactile and touchless interaction in real time,” *Nature Commun.*, vol. 10, no. 1, Sep. 2019, Art. no. 1, doi: 10.1038/s41467-019-12303-5.

[14] T. Le Signor, N. Dupré, and G. F. Close, “A gradiometric magnetic force sensor immune to stray magnetic fields for robotic hands and grippers,” *IEEE Robot. Autom. Lett.*, vol. 7, no. 2, pp. 3070–3076, Apr. 2022, doi: 10.1109/LRA.2022.3146507.

[15] J. Xu et al., “A programmable magnetoelastic sensor array for self-powered human–machine interface,” *Appl. Phys. Rev.*, vol. 9, no. 3, Aug. 2022, Art. no. 031404, doi: 10.1063/5.0094289.

[16] Q. Shu et al., “Magnetic flexible sensor with tension and bending discriminating detection,” *Chem. Eng. J.*, vol. 433, Apr. 2022, Art. no. 134424, doi: 10.1016/j.cej.2021.134424.

[17] S. Xie, Y. Zhang, M. Jin, C. Li, and Q. Meng, “High sensitivity and wide range soft magnetic tactile sensor based on electromagnetic induction,” *IEEE Sensors J.*, vol. 21, no. 3, pp. 2757–2766, Feb. 2021, doi: 10.1109/JSEN.2020.3025830.

[18] C. Becker et al., “A new dimension for magnetosensitive e-skins: Active matrix integrated micro-origami sensor arrays,” *Nature Commun.*, vol. 13, no. 1, Apr. 2022, Art. no. 1, doi: 10.1038/s41467-022-29802-7.

[19] X. Zhang, H. Hu, D. Tang, C. Zhang, J. Fu, and P. Zhao, “Magnetic flexible tactile sensor via direct ink writing,” *Sens. Actuators A, Phys.*, vol. 327, Aug. 2021, Art. no. 112753, doi: 10.1016/j.sna.2021.112753.

[20] X. Guan et al., “Flexible piezoresistive sensors with wide-range pressure measurements based on a graded nest-like architecture,” *ACS Appl. Mater. Interface*, vol. 12, no. 23, pp. 26137–26144, Jun. 2020, doi: 10.1021/acsami.0c03326.

[21] Y. Wei et al., “Fully paper-integrated hydrophobic and air permeable piezoresistive sensors for high-humidity and underwater wearable motion monitoring,” *NPJ Flexible Electron.*, vol. 7, no. 1, p. 13, Mar. 2023, doi: 10.1038/s41528-023-00244-5.

[22] T. Zhao, L. Yuan, T. Li, L. Chen, X. Li, and J. Zhang, “Pollen-shaped hierarchical structure for pressure sensors with high sensitivity in an ultrabroad linear response range,” *ACS Appl. Mater. Interface*, vol. 12, no. 49, pp. 55362–55371, Dec. 2020, doi: 10.1021/acsami.0c14314.

[23] C. Lv et al., “Ultrasensitive linear capacitive pressure sensor with wrinkled microstructures for tactile perception,” *Adv. Sci.*, vol. 10, no. 14, May 2023, Art. no. 2206807, doi: 10.1002/advs.202206807.

[24] M. Farman, R. Prajesh, A. K. Upadhyay, P. Kumar, and E. Thouti, “All-polydimethylsiloxane-based highly flexible and stable capacitive pressure sensors with engineered interfaces for conformable electronic skin,” *ACS Appl. Mater. Interface*, vol. 15, no. 28, pp. 34195–34205, Jul. 2023, doi: 10.1021/acsami.3c04227.

[25] N. Bai et al., “Graded interlocks for iontronic pressure sensors with high sensitivity and high linearity over a broad range,” *ACS Nano*, vol. 16, no. 3, pp. 4338–4347, Mar. 2022, doi: 10.1021/acsnano.1c10535.

[26] Y. Yan et al., “Soft magnetic skin for super-resolution tactile sensing with force self-decoupling,” *Sci. Robot.*, vol. 6, no. 51, Feb. 2021, doi: 10.1126/scirobotics.abc8801.

[27] H. Hu et al., “Wireless flexible magnetic tactile sensor with super-resolution in large-areas,” *ACS Nano*, vol. 16, no. 11, pp. 19271–19280, 2022, doi: 10.1021/acsnano.2c08664.

[28] Y. Li et al., “Origami NdFeB flexible magnetic membranes with enhanced magnetism and programmable sequences of polarities,” *Adv. Funct. Mater.*, vol. 29, no. 44, Nov. 2019, Art. no. 1904977, doi: 10.1002/adfm.201904977.

[29] Y. Zhao et al., “Fully flexible electromagnetic vibration sensors with annular field confinement origami magnetic membranes,” *Adv. Funct. Mater.*, vol. 30, no. 25, Jun. 2020, Art. no. 2001553, doi: 10.1002/adfm.202001553.

[30] Z. Xia et al., “Contact shape and pose recognition: Utilizing a multipole magnetic tactile sensor with a metalearning model,” *IEEE Robot. Autom. Mag.*, vol. 29, no. 4, pp. 127–137, Dec. 2022, doi: 10.1109/MRA.2022.3198372.

[31] H. Dai et al., “Split-type magnetic soft tactile sensor with 3D force decoupling,” *Adv. Mater.*, vol. 36, no. 11, Mar. 2024, Art. no. 2310145, doi: 10.1002/adma.202310145.

[32] X. Zhang, C. Zheng, Y. Li, Z. Wu, and X. Huang, “Magnetically levitated flexible vibration sensors with surficial micropyramid arrays for magnetism enhancement,” *ACS Appl. Mater. Interface*, vol. 14, no. 33, pp. 37916–37925, Aug. 2022, doi: 10.1021/acsami.2c08734.

[33] S. Ding et al., “Sweeping-responsive interface using the intrinsic polarity of magnetized micropillars for self-powered and high-capacity human–machine interaction,” *Nano Energy*, vol. 102, Nov. 2022, Art. no. 107671, doi: 10.1016/j.nanoen.2022.107671.

[34] Q. Zhou et al., “Magnetized microcilia array-based self-powered electronic skin for micro-scaled 3D morphology recognition and high-capacity communication,” *Adv. Funct. Mater.*, vol. 32, no. 46, Nov. 2022, Art. no. 2208120, doi: 10.1002/adfm.202208120.

[35] Y. Yan, Y. Shen, C. Song, and J. Pan, “Tactile super-resolution model for soft magnetic skin,” *IEEE Robot. Autom. Lett.*, vol. 7, no. 2, pp. 2589–2596, Apr. 2022, doi: 10.1109/LRA.2022.3141449.

[36] Y. Xu, B. Wang, X. Hu, and L. Jiang, “A CMOS front-end Hall sensor microsystem for linear magnetic field measurement with best tradeoff between sensitivity and SNR,” *IEEE Trans. Instrum. Meas.*, vol. 71, pp. 1–8, 2022, doi: 10.1109/TIM.2022.3142746.

[37] S. Potukuchi, V. Chinthapenta, and G. Raju, “A review of NDE techniques for hydrogels,” *Nondestruct. Test. Eval.*, vol. 38, no. 1, pp. 1–33, Jan. 2023, doi: 10.1080/10589759.2022.2144304.

[38] U. B. Gunatilake, Y. Alvarez-Braña, E. Ojeda, L. Basabe-Desmonts, and F. Benito-Lopez, “Underwater magneto-driven air de-bubbler,” *J. Mater. Chem. A*, vol. 10, no. 24, pp. 12832–12841, 2022, doi: 10.1039/d2ta01009g.

Xuejiao Li received the B.S. degree from the College of Information and Computer, Taiyuan University of Technology, Taiyuan, China, in 2022. She is currently pursuing the M.S. degree in integrated circuit engineering with the School of Integrated Circuits and Electronics, Beijing Institute of Technology, Beijing, China.

Her current research interests include hall sensors and magnetic tactile sensors.

Runyi Deng received the B.S. degree from the School of Mechanical Engineering, Hebei University of Technology, Tianjin, China, in 2021. She is currently pursuing the Ph.D. degree in mechatronic engineering with the School of Mechanical Engineering, Zhejiang University, Hangzhou, Zhejiang, China.

Her current research interests include multipole magnetization and magnetic tactile sensors.

Wenlong Jiao received the Ph.D. degree in mechanical engineering from Northwestern Polytechnical University, Xi'an, China, in 2018.

He is a Senior Engineer at BIT Chongqing Institute of Microelectronics and Microsystems, Chongqing, China. His research interests include micromirrors, piezoelectric sensors, pressure sensors, uncooled IRFPA, and MEMS CAD.

Shizhen Xu received the B.S. degree from the School of Materials Science and Engineering, Beijing Institute of Technology, Beijing, China, in 2023, where he is currently pursuing the M.S. degree in integrated circuit engineering with the School of Integrated Circuits and Electronics.

His current research interests include microfabrication/nanofabrication technology and CMOS-MEMS sensors.

Huikai Xie (Fellow, IEEE) has been a Professor at the School of Integrated Circuits and Electronics, Beijing Institute of Technology, Beijing, China, since 2020. He has published over 300 technical articles and 11 book chapters and holds over 30 U.S. patents and over 40 Chinese patents. His current research interests include microelectromechanical systems (MEMS)/nanoelectromechanical systems (NEMS), optical beam steering, optical communications, LiDAR, near-infrared spectroscopy (NIR) spectroscopy, and optical microendoscopy.

Prof. Xie is a Fellow of the Society of Photo-Optical Instrumentation Engineers (SPIE). He is an Associate Editor of the IEEE Sensors Letters and *Sensors and Actuators A: Physical*.

Dong Han received the Dr.Eng. degree from Tokyo Institute of Technology (Tokyo Tech), Tokyo, Japan, in 2018.

From 2018 to 2020, he joined the Laboratory for Future Interdisciplinary Research of Science and Technology (FIRST), Tokyo Tech, as an Assistant Professor. In 2020, he worked for the School of Mechanical Engineering and State Key Laboratory of Fluid Power and Mechatronic Systems, Zhejiang University, Hangzhou, China, as a Research Professor. His research interests include intelligent tunnel boring machine electrohydraulic control systems, electromagnetic, piezoelectric, functional fluid drive systems, and medical device development.

Xiaoyi Wang (Member, IEEE) is currently an Associate Professor with the School of Integrated Circuits and Electronics, Beijing Institute of Technology, Beijing, China. He has published more than 50 international journal and conference papers including IEEE Journal of Solid-State Circuits (JSSC), IEEE Transactions on Industrial Electronics (TIE), IEEE Journal of Microelectromechanical Systems (JMEMS), IEEE Transactions on Instrumentation and Measurement (TIM), IEEE Transactions on Electron Devices (TED), *Microsystems and Nanoengineering*, *ACS Applied Materials and Interfaces* (AMI), *Flexible Electronics*, IEEE MEMS, and Transducers. His research interests mainly focus on the CMOS-MEMS monolithic integrated artificial intelligent sensors equipped with artificial intelligence (AI) technology for physical/chemical information sensing, storage, process, and analysis including structural health monitoring sensors, environmental sensing hubs, gas sensor arrays, and electric power sensing units. He also focuses on microfabrication/nanofabrication technology, soft electronics, integrated microsystems, and their applications in industries, smart homes, and healthcare.